Engineering Structures 352 (2026) 122113

Contents lists available at ScienceDirect

Engineering Structures

journal homepage: www.elsevier.com/locate/engstruct

An enriched and phenomenologically sound multilaminate model for masonry: JMM-E

Marialuigia Sangirardi [a,*], Giacomo Di Santo [b], Angelo Amorosi [b]

[a] University of Oxford, Department of Engineering Science, Oxford OX1 3PJ, UK
[b] Sapienza Università di Roma, Department of Structural and Geotechnical Engineering, Via Eudossiana 18, Rome, Italy

ARTICLE INFO

Keywords:
Masonry
Anisotropy
Damage
Plasticity
Multilaminate

ABSTRACT

Masonry is a composite material, whose structural response is strongly influenced by its internal structure: the organised or random arrangement of units and mortar joints in a periodic pattern. A distinctive feature of its constitutive behaviour, in case of organised texture, is anisotropy. In the context of multilaminate constitutive formulations, this paper proposes an enriched version of the Jointed Masonry Model (JMM). Holding the same fundamental hypotheses of elastic-perfectly plastic behaviour of its predecessor, the updated model entails a phenomenological approach, which accounts for possible failure mechanisms at the macroscopic scale and, accordingly, defines the yield domains on preferred, fixed orientations. The paper presents the mathematical formulation of the enhanced model (JMM-E), its response in case of specific stress conditions for a representative volume, and its validation against well documented experimental tests. The model is implemented in a finite element software and features a relatively simple calibration, on which a detailed discussion is presented, also providing standard references in case of both existing and new constructions.

1. Introduction

Masonry is the most ancient construction technique, resulting from the organised or random assemblage of natural (stones) or fabricated (bricks) units, bonded by mortar or by pure friction (as in the case of dry joints) at their contact.

The structural behaviour of masonry is governed by the geometry of its internal structure, the mechanical properties of its components, and by the bond between them. Consequently, it is as complex as variable their combination can be (Fig. 1). Distinctive features can be generally recognised: low tensile strength, high compressive strength, and anisotropy.

Both units and mortar are characterised by brittle response in tension and in compression, the latter showing a markedly higher strength. The bond between them is usually weak; its behaviour can be described by a frictional law in shear (with some cohesive contribution in case of joints filled with mortar and cohesion close to zero in case of dry joints) and a purely cohesive law in tension.

As extensively discussed in the scientific literature, a key ingredient of masonry structural response is anisotropy [1–3]. This can be either recognised in the elastic properties of the material or in the form of strength anisotropy, meaning that strength properties of masonry differ not only in tension and compression, but also along different directions. This effect is particularly evident in case of regularly bonded masonry with periodic texture. Conversely, for more disordered patterns (typically in natural stones assemblages) anisotropic stiffness and strength fade because of the loss of internal structure periodicity.

The description of such complex structural response is challenging and alongside a progressively wider availability of powerful computational resources, several approaches were proposed [4,5].

Limiting the discussion to the Finite Element Method (FEM), masonry can be modelled following micromechanical (simplified or detailed if units, mortar joints and the interface between them are all individually modelled) (e.g. [6–8]) or macromechanical approaches (e.g. [9–12]). The latter assume that masonry is described as a continuum, whose properties can be deduced from tests on assemblages or by homogenisation procedures that derive the composite properties from the constituent ones [13–18] to cite some. In spite of the increasingly powerful hardware resources available, the computational effort required by micromechanical approaches is still very high and, despite allegedly providing the most realistic representation of the actual masonry structural behaviour, their application to real-scale engineering

* Corresponding author.
E-mail addresses: marialuigia.sangirardi@eng.ox.ac.uk (M. Sangirardi), giacomo.disanto@uniroma1.it (G. Di Santo), angelo.amorosi@uniroma1.it (A. Amorosi).

https://doi.org/10.1016/j.engstruct.2026.122113
Received 11 August 2025; Received in revised form 4 December 2025; Accepted 5 January 2026
Available online 10 January 2026

boundary value problems is not routinely considered. Only few studies report the successful use of distinct element modelling approach (DEM) to the analysis of majestic structures in seismic conditions [19] Macro-mechanical approaches allow compromising between accuracy and calculation efficiency and are thus preferred, especially in the context of full-scale problems [20]. Among the numerous constitutive models developed for masonry, those that account for the material's anisotropy provide significantly improved predictions of failure mechanisms [12, 21–23].

Under specific conditions, such as periodicity, dimensions of the units much smaller than the dimensions of the structure, strong units and weak joints, masonry can be looked at as a multilaminate continuum with preferred failure orientations. Multilaminate framework [24–26] is based on the slip theory and on the feature that the constitutive models respond to the rotation of principal stress axes. In the multilaminate idealisation, a material point is surrounded by an infinite number of randomly oriented planes in space, candidate to contributing to inelastic deformation. Accordingly, the strain regime in the continuum can be deduced from the description of sliding, separation or closing phenomena under the current state of stress that can, in principle, occur over any of the randomly oriented planes. However, sliding can take place only on a limited number of planes under a given state of stress and the global inelastic strains are the sum of the contributions provided by active planes. In this context, models can be formulated to account for a finite number of failure planes [27], suited for those cases in which preferred failure orientations can be identified as a consequence of an organised internal structure (as in the case of masonry) or of the appearance of multiple layers. This is the case of natural geomaterials as sedimentary rocks (shale, limestone, and mudstone), formed by deposition and characterised by subsequent specific orientation patterns. Hence, the Jointed Rock Model (JRM) [28] was formulated to simulate the response of materials in which a set of discontinuities/preferred failure orientation can be recognised and is expected to affect the behaviour of the rock mass. Originally, this model was meant to account for a set of three orientations.

Along the same fundamental hypotheses of the Jointed Rock Model, a constitutive model for masonry, named Jointed Masonry Model (JMM), was formulated and implemented in the Finite Element code PLAXIS 3D [29]. It stems from the idea that, in most cases, failure in masonry structures occurs along its bed (horizontal) and head (vertical) joints, that can thus be treated as preferred failure orientations, just like weak planes in layered rock formations (Fig. 2). This is particularly true in case of "strong units and weak joints" [30–34], that is in case of units showing a markedly higher strength with respect to mortar (and of the bond between them). Such condition holds, by definition, in case of dry masonry, and for most brick-mortar assemblages. The JMM accounts for the so-called pseudo-tensile strength induced by staggering joints and its vertical stress-dependency by means of additional terms in the equations defining the strength domains on the head joints plane. This model was used to analyse several soil-structure interaction problems at the scale of the full structures [35–37].

This paper proposes a modified (enriched and phenomenologically sound) version of the JMM model: JMM-E. The novelty introduced with respect to its predecessor is threefold. Firstly, the formulation of JMM-E is enriched by a more rigorous definition of the failure mechanisms accounted in the representative volume element (RVE) and three-dimensional strength domains are introduced for a more robust and clearer interpretation of the constitutive behaviour, setting mechanically consistent thresholds for strength increments and accounting for four possible limit configurations. Secondly, several output variables are introduced and can be extracted during the analysis to understand the orientation associated with the onset of plasticity, offering a more insightful description of the occurring damage mechanisms. Thirdly, the calibration procedure (which involves a limited number of mechanically interpretable parameters) is described in detail, showing possible strategies and standardised test procedures that can be used for either new or existing structures (for which calibration of constitutive models is known to be a rather difficult process).

In light of the above discussion, the main advantages of the use of the proposed model lie in the computational cost (which is in line with other macromechanical approaches and comparatively small with respect to that demanded by micromechanical constitutive models), in the ease of calibration, for which an intuitive and standards-based approach is proposed, and in the wealth of output information available.

The paper is organised as follows: Section 2 introduces the model formulation. Section 3 presents idealised analyses on representative volume elements subjected to uniaxial, simple shear, and multiaxial stress state. Section 4 describes the calibration procedure, while Section 5 presents validation analyses on experimental tests on masonry walls with and without openings, discussing the insights provided by the available output. The interested reader can find the results of numerical simulations performed adopting the JMM model on the same case study in the work by Lasciarrea et al. [29], though it should be noted that results may differ also in light of the different constitutive parameters adopted. A comparison on equal terms of JMM-E and its predecessor is eventually presented in Section 6, where an idealised tunnelling scenario is analysed and the same constitutive parameters, tuned on a realistic masonry material are used. Conclusions and future developments are eventually presented in Section 7.

2. Formulation of the updated model

The JMM-E is an elastic-perfectly plastic model formulated in the framework of multilaminate plasticity. As the JRM and the JMM, the validity of some basic hypotheses needs to be firstly introduced to adopt this constitutive description of the heterogeneous material as a homogenised continuum with preferential and pre-determined (fixed) failure orientation.

Fig. 1. (a) Mixed stone-brick masonry wall in Greece, (b) historic cottage in Oxfordshire (UK), (c) dry-stone masonry wall in Apulia (Italy).

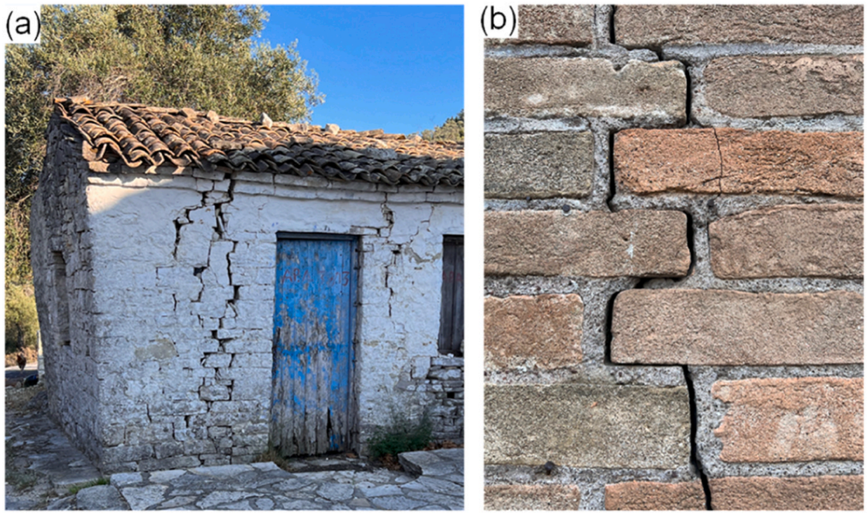

Fig. 2. (a) Damage on a dry-joints stone masonry house in Paxos island (Greece), (b) tensile failure on head joints in a brick masonry wall in Rome (Italy).

A fundamental assumption, justifying the use of a multilaminate approach, is that the material exhibits an anisotropic behaviour. Anisotropy, as briefly mentioned in the Introduction, arises when the internal structure of the material is sufficiently "organised", resulting in the fact that the orientation of weak planes can be identified in the bond pattern. In masonry walls, these planes usually coincide with horizontal and vertical ones, perpendicular to the wall face, while rubblestone masonry, because of the commonly disordered arrangement of stone units, has a substantially isotropic behaviour, thus not suitable for a "multilaminate interpretation" with a limited (two for the presented model) number of planes.

The internal structure of the parent heterogeneous medium needs to be regular and, thus, periodic, to allow the definition of homogenised properties, expected to describe the behaviour of the equivalent continuum material. This periodicity allows to identify stiffness and strength properties of a RVE and to assume their validity for the whole volume of the analysed structure.

Another important aspect of the proposed approach lays in a scale issue: it is assumed that the dimensions of the units (their width b and their height a) are much smaller than a representative dimension of the structure (for example, the height of a wall H). If this condition holds, the multilaminate idealisation, which assumes that an infinite number of parallel failure planes are present for each preferred orientation, can be adopted.

2.1. Definition of failure planes and their orientation

A single-leaf masonry wall with a running bond is depicted in Fig. 3a. In this case, two orientations on which failure can occur are identified; these coincide with the horizontal, i.e. failure can occur on bed joints, and with the vertical one, assuming the other "weak" plane is the head joints one. A schematic representation of the simplified continuum material resulting from the homogenisation of the elastic properties and the definition of two infinite series of horizontal and the vertical planes is reported in Fig. 3b. When setting the properties of the model, the orientation of each series of planes needs to be defined. At this scope, a global three-dimensional cartesian reference system xyz is introduced as well as a local one nst. n is the normal axis, s is the fall axis, and t is the horizontal axis. By convention, t is always assumed to be restricted to the horizontal plane. Two angles completely define the position of a generic plane π (representative of an orientation): the dip α_1 and the strike α_2 (Fig. 3c). α_1 is the angle measured, on a vertical plane, between s and its

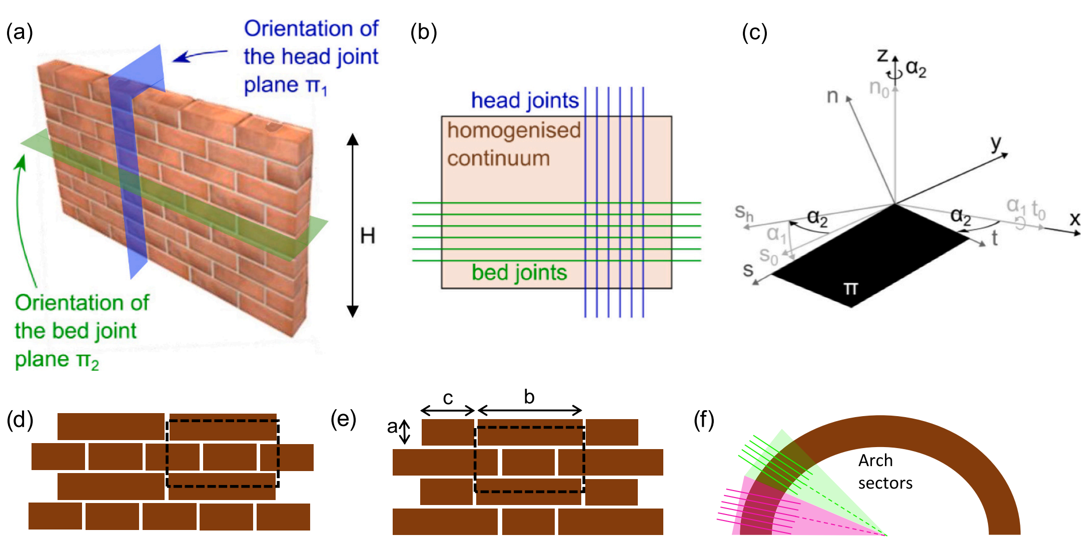

Fig. 3. (a) A running bond masonry panel and the orientation of head and bed joints planes, (b) schematic representation of the idealised continuum with infinite parallel planes along the two selected orientations, (c) definition of the dip and the strike angle of a generic plane π in a global reference system; (d) English bond RVE, (e) Flemish bond RVE, (f) definition of failure planes orientation for arched structures.

projection s_h on the horizontal plane xy, and it is positive for a positive rotation around the t axis. α_2 is the angle between the global x axis and t, and it is positive in case of a negative rotation around the global z axis.

While the definition of dip and strike angles is straightforward in the case of bed joints ($\alpha_1 = \alpha_2 = 0$), it deserves some caution when the head joints plane is concerned, as the position of the wall in the global reference system influences the value of α_2 (for vertical walls and vertical head joints α_1 is always equal to $\pi/2$).

The definition of failure orientations (and of the associated yield domains) requires some further attention for other bond patterns, or curved structures. In the case of English (Fig. 3d) or Flemish (Fig. 3e) bond, failure orientations remain parallel to the horizontal (bed) and to the vertical (head) planes, but a new RVE should be identified, and consequent strength properties on each orientation need to be derived. The model can also be used in the case of masonry arches, activating a single plane and reasonably disregarding any interlocking effect; joints will be interpreted as parallel planes within pre-determined arch sectors (Fig. 3f).

In the following, the model formulation and the validation examples assume a regular running bond texture, but yield domains for different bond patterns can be relatively easily deduced based on analogous considerations.

2.2. Elastic behaviour

The calibration of the linear elastic properties in JMM-E follows the same procedure of its predecessor JMM [29]. The analytical homogenisation adopted is originally presented in [17,38] in a plane stress framework. The elastic constants of the anisotropic homogenised continuum are determined through the following Eqs. (1–4). The constitutive properties of bricks and mortar need to be known as well as the characteristic geometric properties of the representative volume (height of the block a, width of the block b, thickness of the mortar joints t). E_1, the Young's modulus in the direction perpendicular to the head joints, and E_2, the one perpendicular to the bed joints, the shear modulus G and the Poisson's ratios ν_{12} and ν_{21} are calculated as:

$$\frac{1}{E_1} = \frac{4a}{4abK_n + b^2K_t} + \frac{1}{4\mu_b} + \frac{1}{4(\lambda'_b + \mu_b)} \tag{1}$$

$$\frac{1}{E_2} = \frac{1}{aK_n} + \frac{1}{4\mu_b} + \frac{1}{4(\lambda'_b + \mu_b)} \tag{2}$$

$$\frac{1}{G} = \frac{1}{aK_t} + \frac{4a}{b^2K_n + 4abK_t} + \frac{1}{\mu_b} \tag{3}$$

$$\frac{\nu_{12}}{E_1} = \frac{\nu_{21}}{E_2} = \frac{\lambda'_b}{4\mu_b(\lambda'_b + \mu_b)} \tag{4}$$

where the brick elastic properties are expressed in terms of Lamé constants μ_b and λ_b, given by the well-known expressions with respect to E_b and ν_b:

$$\mu_b = \frac{E_b}{2(1 + \nu_b)} \tag{5}$$

$$\lambda_b = \frac{E_b\nu_b}{(1 + \nu_b)(1 - 2\nu_b)} \tag{6}$$

And, in light of the plane stress assumptions, the constant λ'_b is introduced, as reported in [39]:

$$\lambda'_b = \frac{2\lambda_b\mu_b}{(\lambda_b + 2\mu_b)} \tag{7}$$

The normal stiffness (K_n) and the shear stiffness (K_t) of the joints are easily calculated if mortar (E_m, ν_m) and the bricks elastic properties (E_b, ν_b) are known:

$$K_n = \frac{E_mE_b}{t(E_b - E_m)} \tag{8}$$

$$K_t = \frac{G_mG_b}{t(G_b - G_m)} \tag{9}$$

At present, the model is implemented to account for an equivalent average isotropic behaviour, defined by two constants: G and ν, that need to be set as input material parameters by the user.

2.3. Strength domains

JMM-E is originally formulated to account for the plastic yielding (followed by a perfectly plastic behaviour) to occur on a maximum of three different orientations. At present, strength parameters on the third plane are not affected by any "structure effect" and, as such, they coincide with their initial values set by the user, contrarily to what happens on planes 1 (head) and 2 (bed). In the following only two orientations are considered, as the whole set of applications proposed are restricted to single-leaf masonry structures, thus not requiring the activation of the third plane.

Mohr-Coulomb criterion governs the blocks' yielding at the continuum, thus allowing for their failure too. Such circumstance, that should be interpreted as shear failure of the blocks, is excluded in the following, given the preliminary hypotheses of "strong units and weak joints". In the applications presented, this condition is achieved by setting the strength properties of the blocks to dummy values, three or four order of magnitude higher than the ones adopted on the planes 1 (head) and 2 (bed).

The strength domain on each plane is described by a Mohr-Coulomb criterion (f_{fi}) with a tension cut-off (f_{ti}), according to the following expressions, with $i = 1{,}2$:

$$f_{ti} = \sigma_{ni} - \sigma_{ti} \le 0 \tag{10}$$

$$f_{fi} = \tau_i - c_i + \sigma_{ni} \tan\varphi_i \le 0 \tag{11}$$

where σ_{ni} is the normal stress component on the i-th plane, σ_{ti} is the tensile strength, c_i is the cohesion, φ_i is the friction angle and τ_i is the resulting shear stress acting on the i-th plane, calculated from:

$$\tau_i = \sqrt{\tau_{ti}^2 + \tau_{si}^2} \tag{12}$$

In this expression, τ_{ti} and τ_{si} are the shear components on the plane considered, along the t and the s axes (defined in Section 2.1). For the above-mentioned yield conditions (Eqs. 10 and 11) to be satisfied, at each step of the analysis, cartesian stress components are projected on the pre-determined orientations of bed and head joints by means of transformation matrixes whose terms are calculated from the dip and strike angle of each plane.

In principle, the strength parameters characterising the behaviour of a mortar joint can be obtained if appropriate testing is performed (as it will be explained more in detail in the Section 4, dedicated to calibration), that is $\sigma_{ti,0}$, $c_{i,0}$ and $\varphi_{i,0}$ are known. The subscript "0" means that these properties are not accounting for the internal structure and can thus be seen as "intrinsic" or "initial" ones.

In terms of failure mechanisms involving bed and head joints (all to be considered in plane), four configurations can be referred to (Fig. 4). These were chosen as representative of the actual experimental and real field damage observed in brick masonry structures under differential settlements or horizontal loading.

The updated (hereafter also referred to as "actual" or "current") values of σ_{ti} and c_i are calculated imposing equilibrium conditions on a RVE, accounting for the internal geometry. It is assumed that the friction angle is the same on both planes and does not change, thus:

$$\varphi_i = \varphi_{i,0} \tag{13}$$

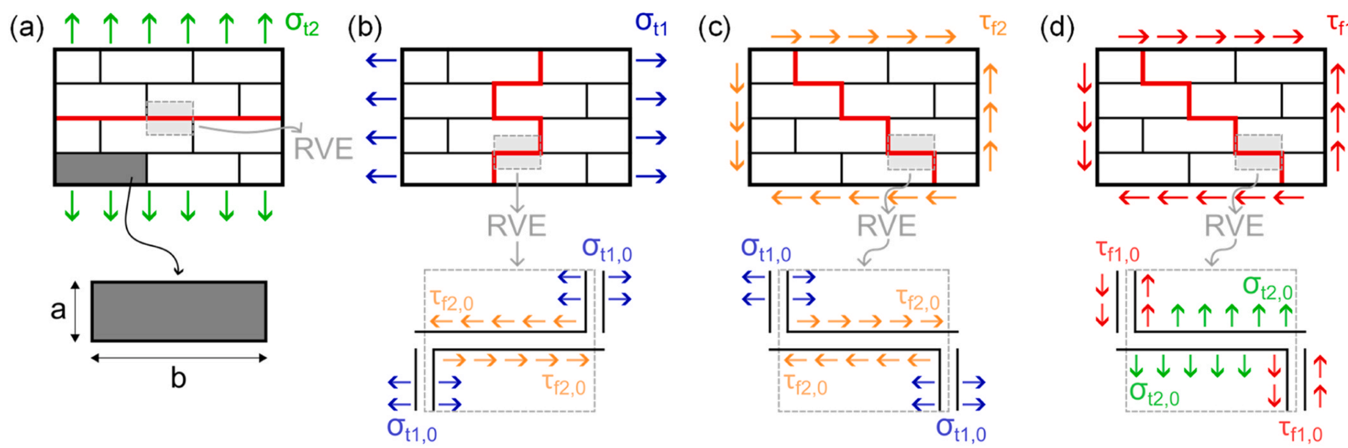

Fig. 4. Failure mechanisms: (a) tensile on bed joints, (b) tensile on head joints, (c) shear on bed joints, (d) shear on head joints.

for $i = 1,2$.

The identified RVE is a rectangle of width equal to $b/2$ and height equal to a. Thickness of the joints is lumped in the brick dimensions and a unit thickness is assumed in the out-of-plane direction.

2.3.1. Tensile strength

Concerning bed joints, the current value of the tensile strength is straightforwardly calculated as the initial one. It is indeed trivial to observe that tensile failure on bed joints (according to the red line in Fig. 4a) occurs if the normal stress exceeds the tensile strength and no other strength contribution is to be considered in this case. Note that the sign convention used throughout the paper identifies tensile stresses as positive. Equilibrium just writes as follows:

$$\sigma_{t2} = \sigma_{t2,0} \tag{14}$$

and the tensile cap in the shear criterion for bed joints is reported in two different reference systems in Fig. 5a and b.

When tensile failure involving head joints is considered, the geometry of the failure (yield) line is reported in red in Fig. 4b. This line follows the internal bond geometry, and tensile failure along head joints can only occur if the shear strength is mobilized along the bed joints. This latter is a function of the initial shear strength properties of the bed joints and of the normal stress acting on them (vertical in the presented cases). This results in a linear increment of the current value of the tensile strength on the head joints, which is provided by the following expression, written on the RVE of height a and width $b/2$:

$$\sigma_{t1} a = \sigma_{t1,0} a + \tau_{f2,0} \frac{b}{2} = \sigma_{t1,0} a + \left(c_{2,0} - \sigma_{n2} \tan\varphi_2\right) \frac{b}{2} \tag{15}$$

having identified with $\tau_{f2,0}$ the shear strength of the bed joints. Rearranging this expression, the term $\beta = \tan\varphi_2 (b/2a)$ is introduced. It quantifies the interlocking effect, and it is an input material parameter, provided the internal structure is inspected and a and b are measured. Eq. (14) thus becomes:

$$\sigma_{t1} = \sigma_{t1,0} + \left(\frac{c_{2,0}}{\tan\varphi_2} - \sigma_{n2}\right)\beta \tag{16}$$

The interlocking-induced increment in the tensile strength, sometimes referred to as the "pseudo-tensile strength" of masonry, is quantified by the second term in the right-hand side of Eq. (15). Remarkably, this increment is proportional to vertical stresses (i.e. normal to the bed joints) and increases when negative values occur (i.e. for compressive stresses); it naturally fades to zero when $\beta = 0$, letting the JMM-E model degenerate into the JRM model.

It should be noted that, for non-zero values of β, a constant increment of the tensile strength arises even in case of zero compressive stress on bed joints. Fig. 5a reports a view of the intersection of the strength domains for the head and the bed joints with the (-σ_{n1}, -σ_{n2}) plane. In the graph, the increment of tensile strength on head joints solely due to cohesion is highlighted and calculated with respect to the initial $\sigma_{t1,0}$. Another critical value reported in this graph is the limit imposed on the maximum value of σ_{t1}. This is a consequence of the Mohr-Coulomb constraint stating that $\sigma_{ti} \leq c_i/\tan\varphi_i$, which should always hold and that is set with respect to the updated and incremented value of cohesion c_1, whose calculation will be clarified in the next Section. Graphically, the limit is reported in Fig. 5c in the (-σ_{n1}, τ_1) plane.

It is specified that the model does not include any compression cap, thus the domain reported in Fig. 5a is only bounded by the tensile strength on the bed joints (horizontal green line), the tensile strength on the head joints (inclined blue line with slope equal to β), and the maximum attainable tensile strength on head joints to comply with Mohr-Coulomb criterion (vertical blue line).

2.3.2. Shear strength

The updated value of the shear strength on bed and head joints planes is calculated starting from the failure mechanisms depicted in Fig. 4c and d. In both cases, the red line marks a stepped mechanism, associated with a pure shear macroscopic state of stress resulting in what is also called "diagonal shear failure". However, in order to formulate

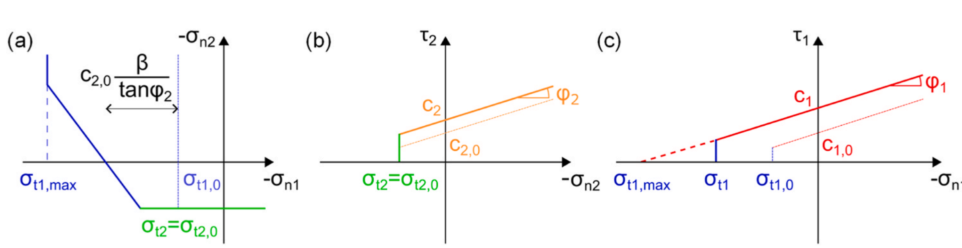

Fig. 5. (a) Strength domain in the (-σ_{n1}, -σ_{n2}) plane, (b) Mohr-Coulomb criterion for the bed joints plane, (c) Mohr-Coulomb criterion for the head joints plane (for a finite stress value σ_{n2}).

the updated strength parameters expressions, we distinguish two conditions: in the first (Fig. 4c) the limiting value of τ_f is equal to τ_{f2}, while in case of head joints shear failure (Fig. 4d) the τ_f is equal to τ_{f1}. It should be observed that the following expressions of τ_{f2} and τ_{f1}, just as those in Eqs. (15–16), aim at accounting for additional strength contributions arising from the geometry of the internal structure and the joints strength that ought to be included in the yield functions associated to oriented planar surfaces.

Similarly to what was done for the tensile strength, here too equilibrium is imposed on the RVE. Referring to Fig. 4c, the current shear strength τ_{f2} is the result of two contributions, one associated with the initial shear strength $\tau_{f2,0}$ and a second one associated with the attainment of the initial tensile strength on head joint. It results:

$$\tau_{f2}\frac{b}{2} = \tau_{f2,0}\frac{b}{2} + \sigma_{t1,0}a = \left(c_{2,0} - \sigma_{n2}\tan\varphi_2\right)\frac{b}{2} + \sigma_{t1,0}a \tag{17}$$

Note that the term associated with the initial value of tensile strength on head joints is constant and, thus, rearranging the expression of τ_{f2}:

$$\tau_{f2} = \left(c_{2,0} + \sigma_{t1,0}\frac{\tan\varphi_2}{\beta}\right) - \sigma_{n2}\tan\varphi_2 \tag{18}$$

an increased value of cohesion c_2 can be obtained by the following:

$$c_2 = c_{2,0} + \sigma_{t1,0}\frac{\tan\varphi_2}{\beta} \tag{19}$$

This results in a vertical translation of the yield line in Fig. 5b, which remains parallel to the initial one ($\varphi_2 = \varphi_{2,0}$).

An analogous calculation can be done to update the current value of the shear strength on the head joints plane (Fig. 4d): imposing the equilibrium on the RVE the following equation holds:

$$\tau_{f1}a = \tau_{f1,0}a + \sigma_{t2,0}\frac{b}{2} = \left(c_{1,0} - \sigma_{n1}\tan\varphi_1\right)a + \sigma_{t2,0}\frac{b}{2} \tag{20}$$

It expresses the current value of the shear strength on the head joints plane as the sum of its initial value plus a contribution arising from the simultaneous attainment of the initial tensile strength on the bed joint. Note that the masonry internal structure enters these expressions by means of the brick dimensions, from which β can be calculated. Rearranging, it results:

$$\tau_{f1} = \left(c_{1,0} + \sigma_{t2,0}\frac{\beta}{\tan\varphi_2}\right) - \sigma_{n1}\tan\varphi_1 \tag{21}$$

The current value of the cohesion on the head joints can be calculated as the sum of two constant contributions:

$$c_1 = c_{1,0} + \sigma_{t2,0}\frac{\beta}{\tan\varphi_2} \tag{22}$$

Similarly to the previous case, this produces a vertical translation of the domain (see Fig. 5c), and the limiting value for the maximum attainable tensile strength on the head joints can be calculated as:

$$\sigma_{t1,\max} = \frac{c_1}{\tan\varphi_1} \tag{23}$$

2.3.3. Three-dimensional domains

Fig. 6 reports the three-dimensional yield domains in the spaces (-σ_{n1}, -σ_{n2}, τ_2) and (-σ_{n1}, -σ_{n2}, τ_1). This clarifies the implications of the above-mentioned equations on the shape of the yield surfaces and offers a graphical interpretation of the bounding strength on bed and head joints.

For a wall orthogonal to one of the cartesian reference axes (so that stress components on preferred orientations are directly deduced from cartesian components of the stress tensor) and in the special, yet common case, of plane stress conditions, the two domains can be merged and represented in a unified reference system (-σ_{n1}, -σ_{n2}, τ), as shown in Fig. 7. This is possible if the out-of-plane component of the shear stress is zero. Considering the expression in Eq. (12), the shear stress τ is equal on bed and head joints. Whether in the gauss point the yield condition is met on the first or on the second orientation, is a result of the complex interplay between internal geometry, initial strength properties, and normal stresses acting on the joints. This will be clarified in the context of the numerical validation of the implemented model, presented in the following Section.

At this point, it is worth it reporting the basic formulae that define the behaviour of the original JMM model, used to reproduce an analogous three-dimensional representation of the yield domain in case of plane stress conditions.

The JMM model assumes that interlocking effects arise when defining the updated tensile strength on head joints, which is expressed by Eqs. (15–16). However, contrarily to what is proposed by JMM-E, the increment in σ_{t1} is accompanied by a “geometrically consistent” increment of cohesion, that is calculated as:

$$c_1 = c_{1,0} - \left(\frac{b}{2a}\sigma_{n2}\tan\varphi_2 - \frac{b}{2a}c_{2,0}\right)\tan\varphi_1 \tag{24}$$

The expression can be further manipulated introducing the term β:

$$c_1 = c_{1,0} - \left(\beta\sigma_{n2} - \frac{\beta}{\tan\varphi_2}c_{2,0}\right)\tan\varphi_1 \tag{25}$$

However, this increment in cohesion, linearly dependent from the compressive stress on bed joints, is not justified by any mechanical consideration. Moreover, the increase in cohesion has the unwanted implication of allowing theoretically infinite increments in the tensile strength of the head joints, since the condition $\sigma_{t1} \leq c_1/\tan\varphi_1$ remains always satisfied. This is, of course, not related to any physical or mechanically compatible phenomenon.

Referring to bed joints, the JMM model does not account for any increment of the shear strength properties, which implicitly understates that only sliding shear mechanisms are possible, without involving tensile failure on head joints. What is above translates into the three-dimensional strength domain reported in Fig. 7b.

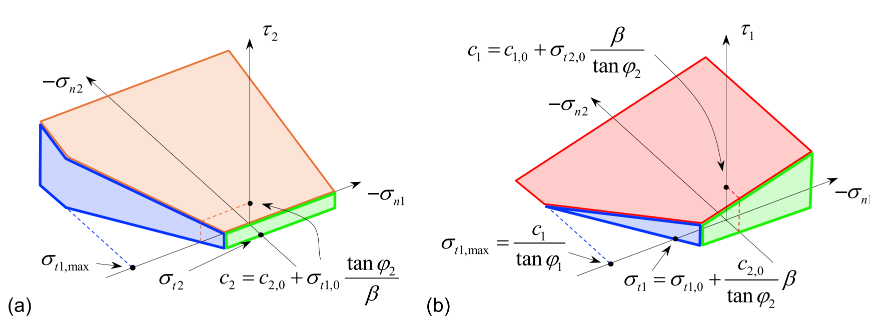

Fig. 6. (a) Three-dimensional yield domain on the head joints plane, (b) three-dimensional yield domain on the bed joints plane.

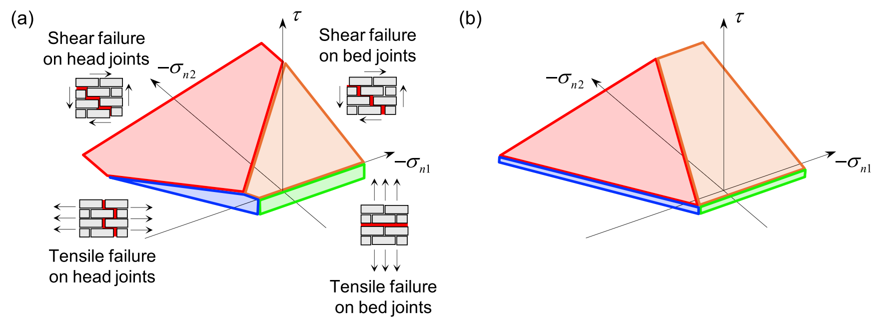

Fig. 7. Combined yield domain for head and bed joints in the reference (-σ_{n1}, -σ_{n2}, τ): (a) JMM-E, (b) JMM.

3. Numerical validation on a representative element of volume

JMM-E was implemented in the commercial finite element code PLAXIS 3D [40] as a user-defined model. Its validation under different stress conditions is first performed in the context of more controllable analyses on a representative element of volume, with the aim of inducing uniform uniaxial or simple shear conditions. The test results will be presented with the support of the above-described domains for better visualization.

Mechanical properties of the REV (Table 1) are deduced from literature [39,41]. The volume reproduces a running bond masonry (as the one depicted in Fig. 3a): given the position of the volume in the three-dimensional reference system, bed joints are parallel to the *xy* plane, while head joints are parallel to *yz* plane. This choice is also particularly convenient for the definition of the dip and the strike angles of the planes, and for the analytical calculation of the stress components on planes 1 and 2, due to the coaxiality of *n*, *s*, and *t* axes of these planes with the cartesian axes. In all the examples presented in the following, the unit weight of the material is set to zero. The effect of self-weight, which would determine a linear increment of vertical stresses in the *z* direction, is controlled by applying a constant normal stress on bed joints so that all points in the RVE are subjected to the same state of stress. In all the simulated tests, a uniform state of strain and stress is induced, thus all gauss points attain failure under the same stress conditions. Out-of-plane kinematic boundary conditions are imposed to eliminate rigid body motions and reproduce plane stress conditions. This is done in a three-dimensional modelling environment, adopting ten-noded tetrahedral finite elements with four integration points.

3.1. Tensile tests

As reported in Section 2.3.1 and according to Eq. (14), the tensile strength on the bed joints is always equal to its initial intrinsic value, thus, albeit trivial, the first validation test consists in subjecting the REV to a displacement in the vertical direction (orthogonal to the bed joints) producing a uniform stress state on the element, as reported in Fig. 8a. Two cases are considered, one in which the normal stress on the head joints (i.e. normal stress in the horizontal direction) is zero, and another for which a non-zero value of σ_{n1} is applied in a first pre-loading step, prior to the application of a vertical displacement. Results in the σ_{n1}-σ_{n2} plane are reported in Fig. 9 and show that the two points representative of the above-described conditions (A and B, respectively) attain failure under different values of σ_{n1}, but meet the yield condition at a constant value of $\sigma_{t2} = \sigma_{t2,0}$.

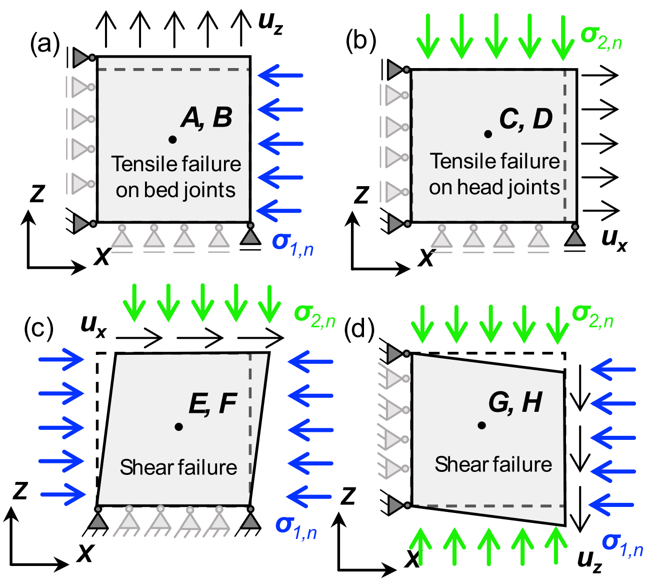

Fig. 8. Boundary conditions used in the representative volume tests: (a) tension on head joints, (b) tension on bed joints, (c) simple shear, (d) alternative configuration for simple shear.

An analogous test is performed with the aim of inducing tensile failure on the head joints. Thanks to the interlocking effect, the tensile strength on this orientation increases proportionally to the normal stress acting on the bed joints. Point C and D represent two different initial conditions: in the configuration reported in Fig. 8b, the value of σ_{n2} is equal to -600 kPa (point C) or equal to -900 kPa (point D). The stress path they are subjected to is reported in Fig. 9 and, in this case, a crucial difference in their response emerges because of the threshold introduced by the JMM-E. Point C attains yield at a value of $\sigma_{n1} = 727.78$ kPa, and this is also the same value at which it would have yielded according to the JMM model. Differently, the stress path of point D intersects the cut-off in tensile strength imposed by JMM-E and thus yields at $\sigma_{n1} = 806.53$ kPa. If JMM had been used, this point would have failed at a higher value of strength (914.11 kPa).

3.2. Simple shear test

To produce simple shear conditions on the representative element of volume, both the configurations reported in Fig. 8c and d can be

Table 1
Mechanical parameters of the JMM-E model adopted for the REV validation analyses.

γ	G	ν	β	$\sigma_{ti,0}$	$c_{i,0}$	φ_i	ψ_i	$\alpha_{1,1}$	$\alpha_{2,1}$	$\alpha_{1,2}$	$\alpha_{2,2}$
kN/m^3	kPa	-	-	kPa	kPa	deg	deg	deg	deg	deg	deg
0	1.04 E+6	0.295	0.636	140	140	23.27	0	90	90	0	0

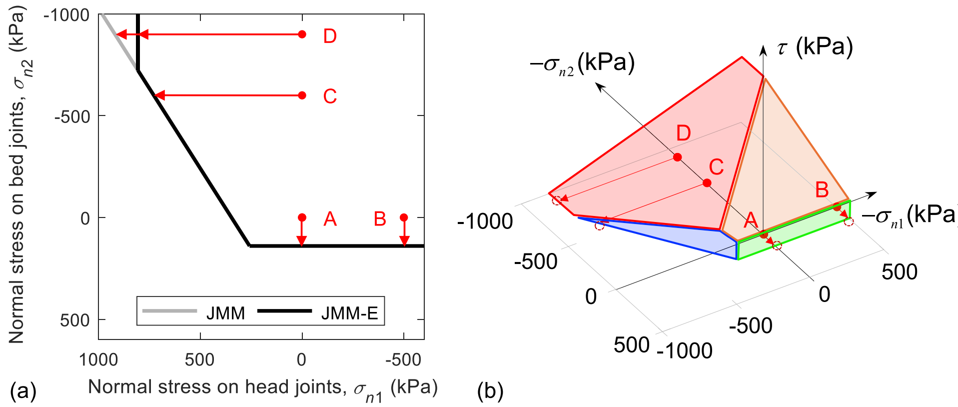

Fig. 9. (a) Stress states after pre-compression phase (red dots) and stress paths up to failure, (b) three-dimensional representation.

adopted. These lead to a uniform shear stress which, for equilibrium, acts on both bed and head joints planes. This implies that whether shear yielding occurs on one of the two orientations is a consequence of the combination of normal stresses and of the geometry of the block (expressed by the ratio $b/2a$).

Note that, for the assumed failure orientations with respect to the cartesian global reference and in light of plane stress conditions

$$\tau_{xy} = \tau_{yx} = \tau_{yz} = \tau_{zy} = 0 \tag{26}$$

it results:

$$\tau_1 = \tau_2 = \tau_{xz} = \tau_{zx} \tag{27}$$

which introduces strong simplifications in the governing equations. Two different initial normal stress conditions are considered, namely point E ($\sigma_{n1} = -200$ kPa, $\sigma_{n2} = -800$ kPa) and point F ($\sigma_{n1} = -500$ kPa, $\sigma_{n2} = -200$ kPa) as reported in Fig. 10. Even if kinematic boundary conditions are different, points G and H in Fig. 8d would follow the same stress path of points E and F, under the same pre-compression stress state.

The shear strength on bed and head joints under the normal stresses represented by point E is 578 kPa and 433 kPa respectively, thus yielding occurs on plane 1, where strength is lower. The normal stresses represented by point F induce shear strength on bed and head joints equal to 320 kPa and 562 kPa, thus yielding occurs on bed joints.

Graphically, this can be observed by looking at Fig. 10a, where the projection of the intersection between the shear domains on both planes is also plotted. Indeed, for constant normal stresses, the stress points E and F move vertically in the three-dimensional stress space (Fig. 10b) under increasing shear deformation, thus their position in the ($-\sigma_{n1}$, $-\sigma_{n2}$) plane (Fig. 10a) can inform on where yielding will occur.

Under the same conditions in terms of normal stresses, the JMM would have led to a different yield condition. In particular, for point E, the shear strength on bed and head joints would have resulted in 484 kPa and 534 kPa, while for point F the same values would be 266 kPa and 499 kPa. This means that in both cases yielding is attained on the bed joints. It can be proven how, in light of the possibly indefinite increment in tensile strength and cohesion on head joints, the JMM model systematically overestimates their shear strength.

4. Calibration of the model

The calibration procedure of the elastic properties of the model is complete once the mechanical properties of the mortar joints and their thickness, the elastic properties of the constituents, the dimensions of the units, and the geometric features of the bond are known. This is normally sufficient if the behaviour is defined as a “strong bricks-weak mortar” one. Alternatively, brick strength properties might need to be determined to define their yield domain (Mohr Coulomb shear + tensile cut-off), which will be used to set bulk failure conditions.

4.1. Elastic properties

For new constructions, determining the Young’s modulus and the Poisson’s ratio of mortar and bricks is relatively easy. It can be done in the context of static tests (compression or flexure tests) using displacement transducers, strain gauges or digital image correlation to evaluate strains, as well as resorting to dynamic methods such as Ultrasonic Pulse Velocity [42] or the Impulse Excitation of Vibration [43]. These latter techniques, albeit originally proposed for concrete materials, can be used in the mechanical characterisation of mortar and bricks, provided some care is used when converting the obtained parameters to their static counterparts, as demonstrated by recent literature [44–47].

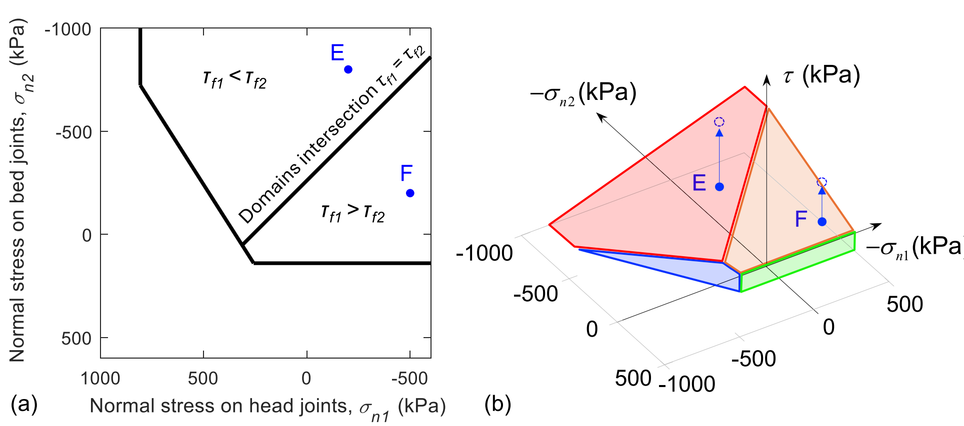

Fig. 10. (a) Stress states after pre-compression phase (blue dots) and (b) three-dimensional representation.

In case of existing structures, the calibration process can be more cumbersome. Units could be extracted and tested *ex-situ*, achieving substantially the same accuracy in elastic characterisation of new materials. Mortar samples that can be extracted from real structures have tight dimensions (as they come from joints whose thickness is usually between 10 and 20 mm) and this prevents the application of standard laboratory tests to determine elastic properties. Usually, compressive strength is determined on site *via* penetrometer tests [48,49] or, if samples are tested in laboratory, by double punch test [50]. However, strength properties of mortar are not in the target of JMM-E calibration, while the strength of the joint is, this latter being mostly related to the bond properties between mortar and units (although some care should be paid, especially when shear strength of the joint is concerned, as it will be discussed later). Penetrometer or punching tests are not suitable for elastic characterisation, unless it is possible to accurately refer to solid relationships between the strength and stiffness of the material (which, to the Authors' knowledge, are generally derived empirically and show marked variability).

An indirect, moderately destructive, but mechanically sound alternative, could involve double flat-jack testing [51]. This test is routinely adopted to first assess the actual state of stress (vertical), in a single-jack preliminary test configuration, followed by the cut of a second slot in which another flat-jack is placed. The inflation of both jacks determines an approximately uniaxial state of stress in the portion of the wall between the two slots. Thanks to vertical displacement transducers, local displacement measures provide an estimate of the induced strains so that the Young's modulus can thus be calculated based on the jacks pressure (i.e., with appropriate conversion, knowing the applied stress).

If the units' properties are known and bond geometry is visible (so that joints number and thickness are visible) a simple analytical calculation could provide a reasonable estimate of the Young's modulus E of the mortar.

4.2. Strength properties

The calibration procedure of the strength properties is aimed at constructing the initial yield domain of the mortar joint, irrespectively, at this stage, of its *future* condition of being a bed or a head joint. In fact, here the basic assumption is that all joints have the same initial properties, and modifications only arise when the internal structure and the actual stress state are considered. At this scope, both tensile (bond) strength and shear strength on joints for different values of the normal stress need to be determined. For new masonry, the initial shear (the values of the friction angle φ and of the cohesion c_0) can be determined following a standardised procedure [52]. Alternative options are also suggested in scientific literature (e.g. [53]).

During these tests, failure of the joint can be attained with different configurations, that is in the unit/mortar bond, in the mortar, in the unit, or with crushing or splitting in the units [52]. The first two modes are the most common in case of strong units and weak mortar (which is the case for which this model has the best performance). Marked evidence of the prevalence of unit failure, as in the two latter modes mentioned above, should highlight the possible inadequateness of JMM-E model to realistically reproduce the overall performance of the studied masonry.

The bond strength, that is the tensile strength σ_{t0} of the joint, can be measured following different standardised procedures, reported in the American Codes [54–56] as well as in [57]. As for the shear strength, alternative, customised options exist (e.g. [58]).

When dealing with existing structures, strength calibration is much more difficult and, to the Authors' knowledge, the only standardised test available to determine shear properties is the shove test, described in [59]. No *in-situ* test procedures are available to determine the tensile strength of mortar joints and thus the only viable options to determine this parameter is either to extract masonry cores or couplets to subject to customised tensile tests *ex-situ*, or to resort to empirical correlations. These latter relate bond strength to mortar mechanical properties, to cohesion of the joint or to physical properties of the bricks such as their permeability. However, bond properties have shown to be not robustly correlated to neither units or mortar strength properties [60]. Indirect determination of tensile strength, as for example those based on the ratio between c_0 and σ_{t0}, should be treated with special care as this ratio can be rather variable as recognised by [61], who recorded values between 1.3 and 7.5. When such ratios are used, attention should be further paid to satisfy the Mohr-Coulomb criterion condition on $\sigma_{t0} \leq c_0/\tan\varphi$.

Until now, no explicit reference was made to dilatancy (ψ_i), which is another material parameter to be set at the input stage. In the following validation analyses the hypothesis of non-associative plastic flow (and in particular $\psi_i = 0$, i.e. no dilation) is made, but the user can arbitrarily input an alternative value (a commonly used and simplified hypothesis is associative plastic flow, implying $\psi_i = \varphi_i$, which was often adopted in past studies based on the JMM model) or refer to specific test results, if these are available (as in the case of the example presented in the following Section).

A synthesis of the calibration procedures described above is summarised in Table 2.

5. Numerical examples

5.1. Shear test on masonry wallets

The model is validated against well-documented pseudo-static and monotonic shear tests on masonry walls, extensively referred to in the scientific literature [62] and numerically simulated adopting different approaches [6,18,63]. These tests were also presented in [29] as a benchmark for JMM model. The reader can refer to those results for comparison. However, the Authors wish to specify that the parameters adopted in this paper are different from those adopted in [29] and result from calibration following the principles described in the previous section and the data available from [61].

The walls have a width/height ratio of about one with dimensions 990 mm × 1000 mm and they are first loaded in the vertical direction to induce compression in the bed joints and then subjected to horizontal loading at the top under displacement control, preventing rotation of the top edge. Two geometries are tested, namely a plain façade (PF, Fig. 11a) and a wall with a central opening mimicking the presence of a window (WF, Fig.11b). They are both built up with 18 courses, from which 16 courses are active and 2 courses are clamped in steel beams [63]. The units used are wire-cut solid clay bricks with dimensions 204 mm × 98 mm × 50 mm and 12.5 mm thick mortar joints [6,61]. In the experiments, different values of vertical precompression stress p, obtained imposing a uniformly distributed force, were first applied, followed by the application of the top displacement d, keeping the bottom and top boundaries horizontal and precluding any vertical movement (Fig. 11a and b). In the following, the tests on plain walls J4D and J5D (two samples with identical geometric and material properties) and the window walls J2G and J3G (identical sample tested for repeatability) are simulated. When global force-displacement are plotted, results of wall J3D (identical to J4D and J5D but for which no crack pattern was available) are also reported. In all the above tests the vertical stress p applied is equal to 0.3 MPa and the analysis is conducted in three steps. First, the model is initialised and boundary conditions to eliminate rigid body motion are applied, together with the activation of self-weight. Then, precompression is applied. In the third step a rigid body constraint to the top surface of the wall is applied as a boundary condition, preventing vertical and out-of-plane displacements and rotations, while normal stress is kept constant and horizontal displacement is applied at the top surface of the wall. The analyses are conducted in the Finite Element software Plaxis 3D and, similarly to what was done for the analyses reported in Section 3, ten-noded tetrahedra are used and boundary conditions are enforced to simulate plane-stress conditions.

The mechanical properties of the material are reported in Table 3 and are consistently deduced from experimental tests performed on

Table 2
Calibration methods for stiffness and strength parameters of the model.

Parameter	E_m, ν_m	E_b, ν_b	b/a, t	σ_{t0}	φ	c_0
New structures	Compression (EN1015–11, EN771–1 A1)Flexural tests(EN1015–11, ASTM C67)		Visual inspection	Bond strength tests (ASTM C952, ASTM C1072, ASTM C1357, EN 1052–5:2005), customised tests (Khalaf et al. 2005)	Initial shear (EN 1052–3:2002), customised tests (Liu et al. 2023)	Initial shear (EN 1052–3:2002), customised tests (Liu et al. 2023)
Existing structures	Indirect calculation from flat jack testing (ASTM C1197–22, RILEM LUM.D.3)	Compression or flexural tests on extracted bricks	Visual inspection	No standard options	Shove test (ASTM C1531–23)	Shove test (ASTM C1531–23)

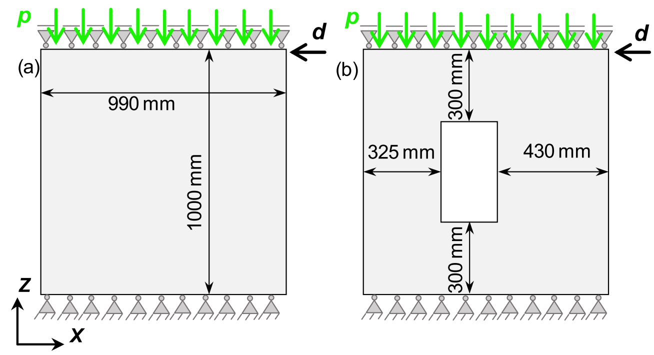

Fig. 11. Geometry and test configuration for: (a) walls J4D and J5D, (b) window walls J2G and J3G.

masonry samples and reported in [61], referring to bricks of type J and mortar of type B. The tests performed include initial shear and tensile tests on masonry couplets. Dilatancy is also deduced from experiments reported in the cited book. Elastic properties of the masonry are calculated from analytical homogenisation following the procedure described in Section 2.2. While tensile strength is directly obtained from test results, and as the lower bound of the measured strength, the value of cohesion is assumed as equal to one fourth of the cohesion measured during tests on triplets. This is justified by the fact that the shear stress-displacement curves reported in [61] show a markedly brittle response with residual shear strength approximately equal to 0.25 of the peak value.

5.2. Results

In the following, results are first reported in terms of global force-displacement data (Fig. 12). In both cases (for PF and WF) the model satisfactorily reproduces the global response of the wall. In particular, the model slightly overestimates the force capacity of the plain façade when the comparison is made with J4D and J5D, while the experimental response of J3D is here considered as an outlier, being much higher in terms of maximum horizontal force, possibly due to different boundary conditions imposed during the precompression phase.

The implemented JMM-E provides a wealth of information in the standard software output, namely a detailed description of the plastic points, that are distinguished between tensile and shear on bed and head joints. Four different symbols are used to indicate gauss point experiencing yielding at the end of each step. Remarkably, these points only appear when the stress state persists on the yield surface and disappear instead in the case of elastic unloading. It is important to keep this in mind since the plastic point distribution is not representative of any accumulated damage. This information can be deduced from other outputs, made available to the user in this new implementation, related to the current plastic strains on the failure planes. When plotting plastic strains, their values are classified according to traditional metrics [64], based on the “ease of repair concept”. It is anticipated that where strain concentrations are, damage can be classified as “severe”.

Additionally, the commercial code in which the model has been implemented allows plotting the history of plastic points, providing a graphical representation of all locations where yielding occurred during the analysis. This enables the user to retrospectively inspect the simulation and identify critical stages by observing the evolution of plastic points step by step.

The original JMM model distinguished plastic points between shear and tensile failures but lacked information about the specific plane of yielding. Users had to post-process the stress state and compare it to the analytically derived yield domain to infer this detail.

Traditionally, damage in masonry structures is assessed via the distribution, intensity, and orientation of maximum principal tensile

Table 3
Mechanical parameters of the JMM-E and JMM model of the Eindhoven walls.

γ	G	ν	β	$\sigma_{ti,0}$	$c_{i,0}$	φ_i	ψ_i	$\alpha_{1,1}$	$\alpha_{2,1}$	$\alpha_{1,2}$	$\alpha_{2,2}$
kN/m^3	kPa	-	-	kPa	kPa	deg	deg	deg	deg	deg	deg
15	1.40 E + 6	0.25	1.5	228	220	37	20	90	90	0	0

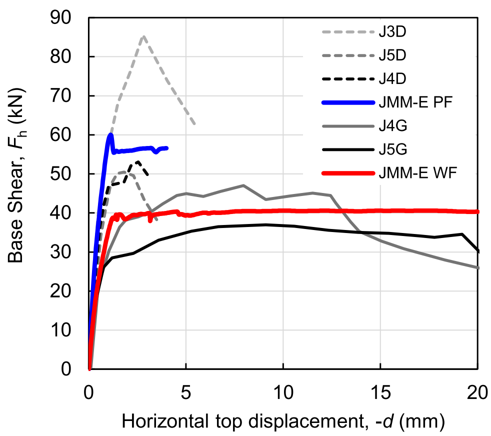

Fig. 12. Global shear-horizontal displacement curves from experiments.

strains. These indicators are also used here to interpret the simulation results.

The experimental results obtained for plain walls J4D and J5D are reported in Fig. 13a and b [63]. Between the two tests, some slight differences in the crack patterns at the end of the experiment can be observed. This demonstrates the difficulty of ensuring repeatability of tests under allegedly identical conditions when masonry structures are concerned. A single simulation is performed adopting the JMM-E model, whose results are reported in Fig. 13c-h. Looking at the distribution of plastic points at the end of the test, it can be noted that it is characterised by the marked prevalence of tensile yield points on head joints (brown) and shear on head joints (blue). This translates in an overall crack pattern characterised by diagonal shear realistically reproducing the observed damage pattern. Interestingly, the maximum principal strains concentrate along the diagonal line going from the bottom left to the right up corner of the panel and at the top left and bottom right corners. Both panel J4D and J5D indeed show horizontal cracks at the same locations and [63] states: "for the lower initial vertical load (walls J4D and J5D), horizontal tensile cracks develop at the bottom and top of the wall at an early loading stage, but, for all the walls, a diagonal stepped crack leads to collapse…". It is not surprising that these horizontal cracks are not evident in the plastic points pattern in Fig. 13c, but it has to be remarked that plastic points at the end of the analysis do not necessarily serve as a proxy of the damage experienced during the entire process but only depict points exceeding yield at that specific stage of the simulation, thus providing no information on the accumulated damage. This information is now available from the plastic strains, coded as an output variable in this model implementation. In particular, the plastic strains should be looked at to understand which kind of permanent deformation (directly related to cracks and damage) has to be expected. At the end of the analysis, normal plastic strains on head joints are concentrated on the diagonal (Fig. 13e), while normal plastic strains on bed joints are concentrated in the top left and bottom right corners (Fig. 13f), where horizontal cracks are marked. Similarly, the shear plastic strains on head joints (Fig. 13g) follow the diagonal shear pattern, while those on bed joints (Fig. 13h) attain their maximum value at the edge of the panel, highlighting the occurrence of high shear strains on the horizontal plane at the contact of the wall with the loading (top) and the retaining (bottom) beams.

Inspecting the plastic points distribution at different stages of the analysis (Fig. 14 a-d) it is possible to detect the correspondence with the

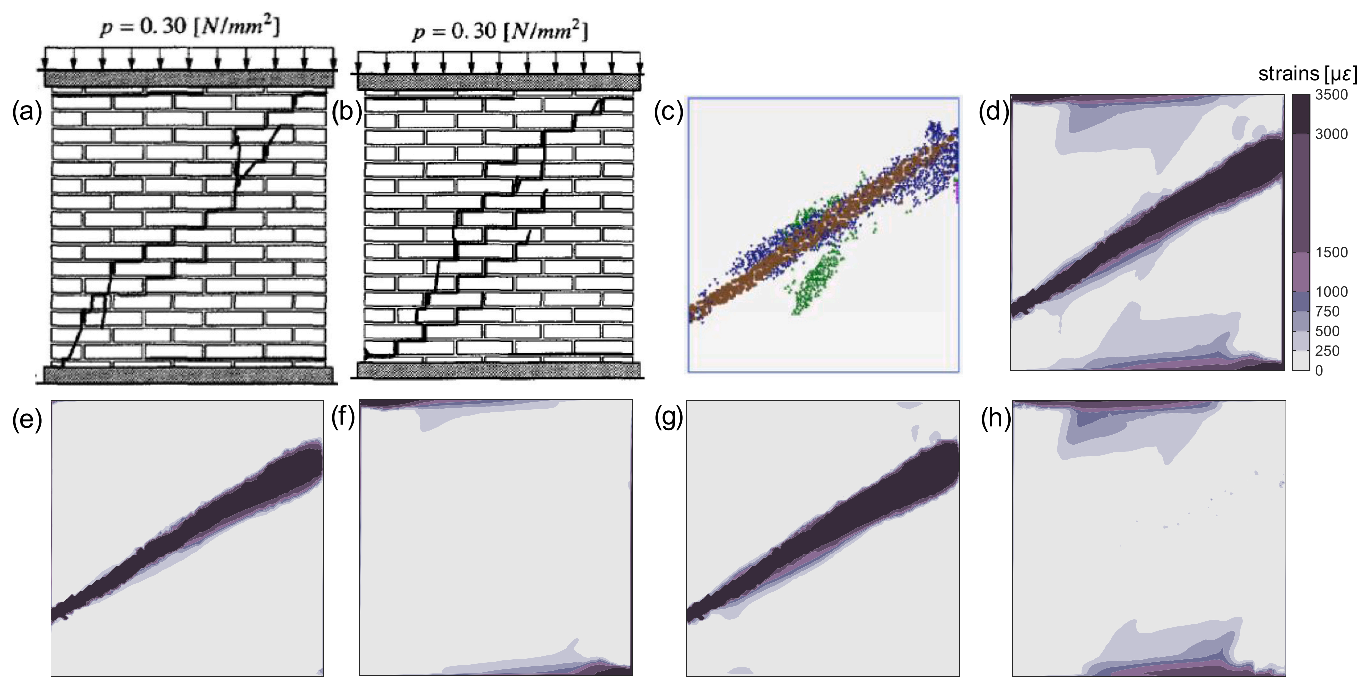

Fig. 13. (a) Crack pattern at the end of test for wall J4D and (b) J5D, (c) plastic points distribution at the end of the simulation, (d) maximum principal strain ε_3, (e) plastic normal strains on head joints $\varepsilon_{p,1}$, (f) plastic normal strains on bed joints $\varepsilon_{p,2}$, (g) plastic shear strains on head joints $\gamma_{p,1}$ and (h) plastic shear strains on bed joints $\gamma_{p,2}$. The colorbar reported in (d) also refers to subfigures e-h.

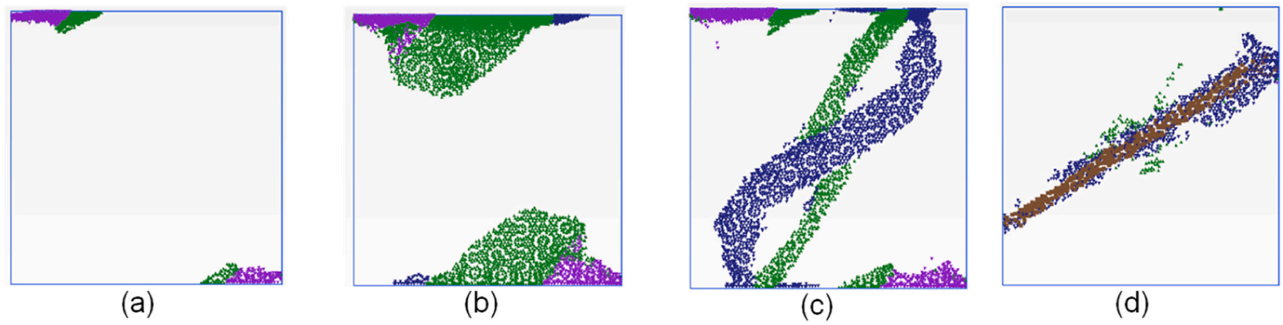

Fig. 14. Plastic points at step (a) 50, d = -0.3 mm, (b) 70, d = -0.8 mm, (c) 90, d = -1.15 mm and (d) 150, d = -2.0 mm.

experiment description reported in [63]. Plastic points first appear as tensile (purple) and shear (green) points on bed joints in the first steps (step 50–70) and later (around step 90) further involve the central part of the wall, mainly highlighting shear yielding. When the displacement reaches -2 mm (step 150) the pattern becomes very similar to the final one. It should be noted that, differently from micromechanical or DEM approaches, this model would not necessarily capture the concentration of plastic processes at the joints locations, in light of its homogenised, macromechanical formulation.

The crack pattern detected at the end of the experiments on the window walls (Figure17 a and b) is less neatly recognisable in the output of the analyses, though the plastic points distribution reported in Fig. 15c and the maximum principal strains Fig. 15d suggest the presence of shear failure essentially concentrated along the diagonal of the wall, initiating at the window corners. This is not in contrast with the experimental evidence, and the damage type descriptors (with tensile failure of head joints also present in the top right part of the wall) provide a realistic indication of the wall response to horizontal actions. Looking at Fig. 15e and f it can be observed how plastic normal strains on head and bed joints concentrate along the diagonal and at the corners of the opening, accordingly to the crack pattern. Plastic shear strains on head (Fig. 15g) and bed joints (Fig. 15h) further confirm the accumulation of residual strains along the diagonal direction. It should be noted that the magnitude of peak plastic strains on head joints are one order of magnitude greater than those on bed joints, though this is not immediately recognisable from Fig. 15 because of the colorbar limits chosen. It is noted that the model leads to a less pronounced concentration of strains, which are instead smeared along the cracking orientations.

The picture of the plastic points distribution taken at different steps of the analysis offers additional information on the evolution of damage. At the first stages (Fig. 16a), plastic points highlight tensile failure on bed joints at the top left and bottom right corners, while shear on bed joints is evident at the top right and bottom left corner of the opening. This condition persists until step 50 (Fig. 16c), when shear failure points appear. At the end of the analysis, the tensile and shear failure on head joints prevails.

Plastic points represent a valuable output of this model, especially considering the newly implemented feature of providing information on which plane is experiencing failure. However, neither maximum principal strains alone, nor plastic points alone, nor the sole combination of the two could provide a comprehensive picture of the damage experienced by the masonry wall. In this context, the plastic strains appear essential to complement the description.

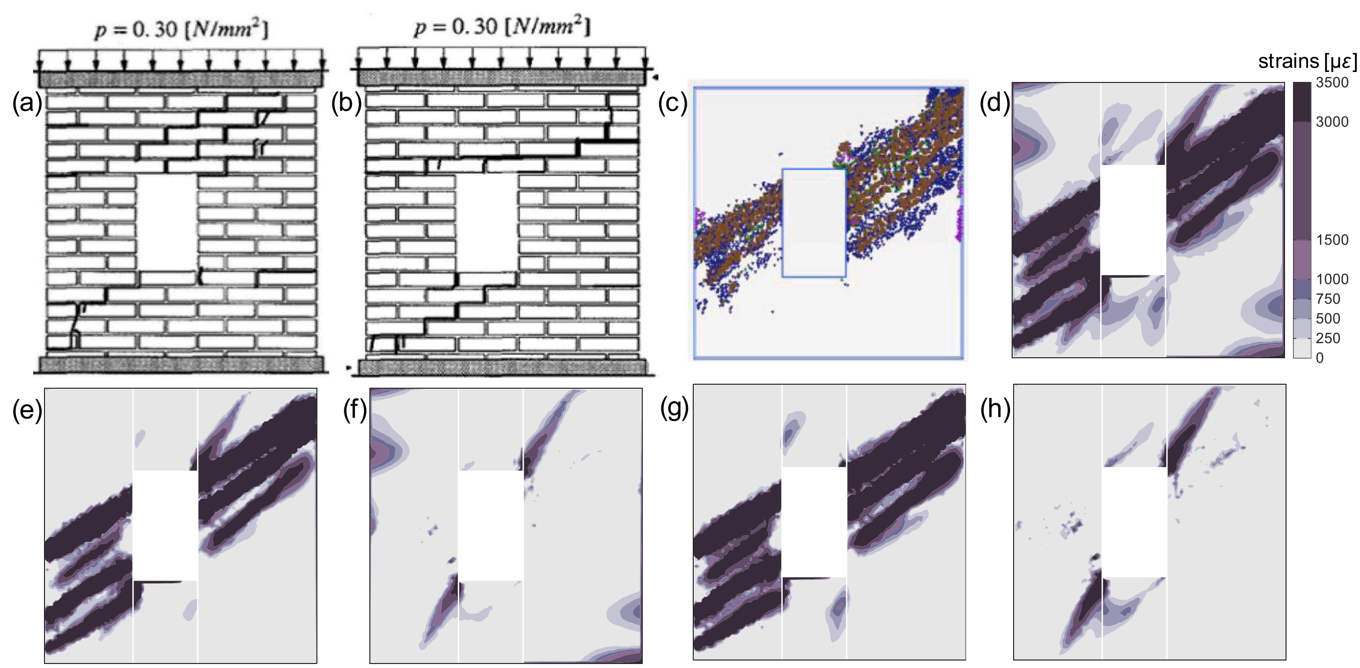

Fig. 15. (a) Crack pattern at the end of test for wall J2G and (b) J3G, (c) plastic points distribution at the end of the simulation, (d) maximum principal strain ε_3, (e) plastic normal strains on head joints $\varepsilon_{p,1}$, (f) plastic normal strains on bed joints $\varepsilon_{p,2}$, (g) plastic shear strains on head joints $\gamma_{p,1}$ and (h) plastic shear strains on bed joints $\gamma_{p,2}$. The colorbar reported in (d) also refers to subfigures e-h.

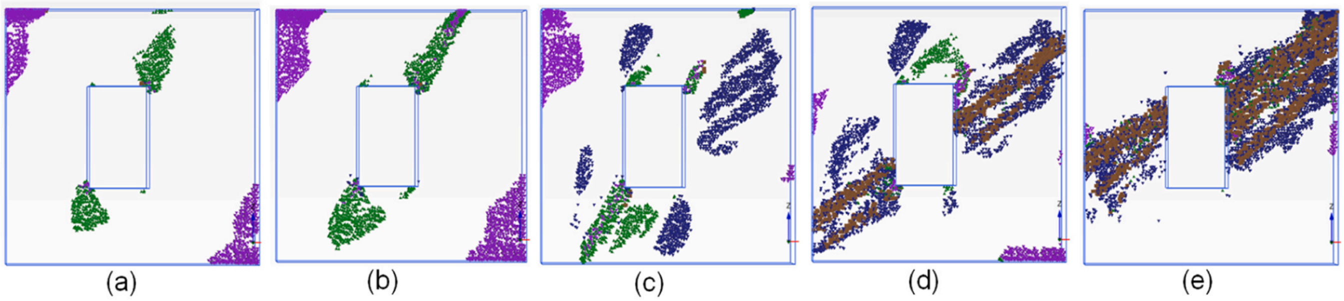

Fig. 16. Plastic points at step a) 20, d = -0.4 mm, b) 31, d = -0.7 mm, c) 50, d = -1.25 mm d) 150, d = -2.7 mm, d) 670, d = -20 mm.

6. Analysis of an idealised tunnelling scenario

6.1. Problem statement

In this case-study, idealised soil stratigraphy and structural configurations are adopted (Fig. 17). The subsoil is characterised by the presence of two horizontal layers: a shallow one made of gravel, extending to a depth of −1.5 m from the ground level. Below, a clay layer extends to a depth of −50.0 m, i.e., the boundary of the model. A circular cross-section tunnel with a diameter equal to 11.0 m is excavated. Its axis is located at a depth of −23.0 m from ground level. A hydrostatic distribution of pore water pressure is assumed, with the water table set at −1.5 m depth. An isolated façade is studied. Its geometry is varies from two to four storey to investigate the influence of its stiffness on the tunnelling-induced damage. The façade is orthogonal and centred with respect to the tunnel axis, and features a foundation beam whose bottom plane is placed in the gravel, at a depth equal to −1.0 m from ground level. Several openings (doors and windows) characterise the geometries and are equipped with lintels, whose behaviour is assumed as elastic. The soil-structure interaction problem is studied through a finite element model built in the geotechnical commercial code PLAXIS 3D. The volume of the subsoil model, above which the façade is located, is 140 m× 20 m× 50 m and is divided into 45983 10-noded tetrahedral elements. The vertical contours are normally fixed, the lower base is fully fixed, and the upper base is free to move. The tunnel excavation is simulated in a single calculation phase (*single-step*) by applying a homothetic contraction and keeping the tunnel invert constrained.

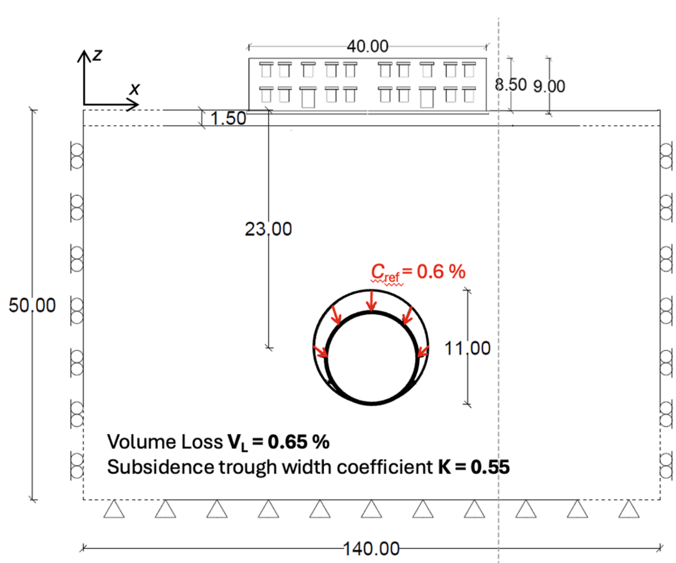

Fig. 17. Schematic representation of the boundary value problem.

A uniform contraction $C_{\text{ref}} = 0.6$ % is applied to the tunnel intrados to reproduce, under free-field conditions, a target analytical settlement trough (a Gaussian distribution curve) characterised by a volume loss $V_L = 0.65$ % and a subsidence trough width coefficient $K = 0.55$. Tunnel lining, foundation beam, and façade lintels are assumed to be isotropic linear elastic. The model is discretised by means of 10-noded tetrahedra except for the tunnel lining, for which 6-noded plate-type elements are adopted. Interfaces are placed between the tunnel and soil and at the contact between the footing and the embedded portion of the façade with the surrounding soil. Clay behaviour is considered undrained throughout the analysis.

The reader is referred to [65] for further details on the constitutive model adopted for the soil, and for the constitutive parameters of gravel, clay, and tunnel lining. For the lintels, an isotropic linear elastic assumption is made, and they are assigned the same stiffness as the masonry material. Table 4 summarises the constitutive properties adopted for both JMM and JMM-E simulations. Dip and strike angles are set according to the orientation of the façade in the global three-dimensional reference reported in Fig. 17.

6.2. Results

The results of the numerical simulations are here reported at the final step of the analysis, i.e. after the tunnel is excavated, in terms of “standard” maximum principal strain output and plastic points. These latter are distinguished between shear and tensile ones and further associated with the plane orientation on which the yield criterion is met. While in the newly implemented JMM-E this information was made available as a standard output of the software, the JMM did not have this feature and plastic points plots for this model are assigned to a specific plane via a semi-automated post-processing coded in MATLAB, in which the state of stress at each gauss point is evaluated against the current yield conditions defined at that specific location (in light of the stress-dependency of the model). For consistency and for rapid comparison, results for the JMM-E are plotted adopting the same formatting convention.

As mentioned, two different geometries are considered, a two-storey and a four-storey façade, the latter being more influenced by the vertical stress dependency of the yield domain.

Looking at Fig. 18, it can be noted that both the JMM and the JMM-E provide a similar damage pattern if maximum principal strains are looked at (Fig. 18a and b); in both cases, damage, classifiable as slight to moderate if the standard damage categories convention is adopted, is mainly concentrated on the spandrels just above the door openings. However, the JMM model fails to recognise additional light damage on

Table 4
Constitutive properties of JMM and JMM-E adopted for the masonry façade.

γ kN/m^3	G kN/m^2	ν -	$c_{i,0}$ kN/m^2	φ_i °	ψ_i °	$\sigma_{ti,0}$ kN/m^2
23.75	755.1E3	0.13	100	30	0	50

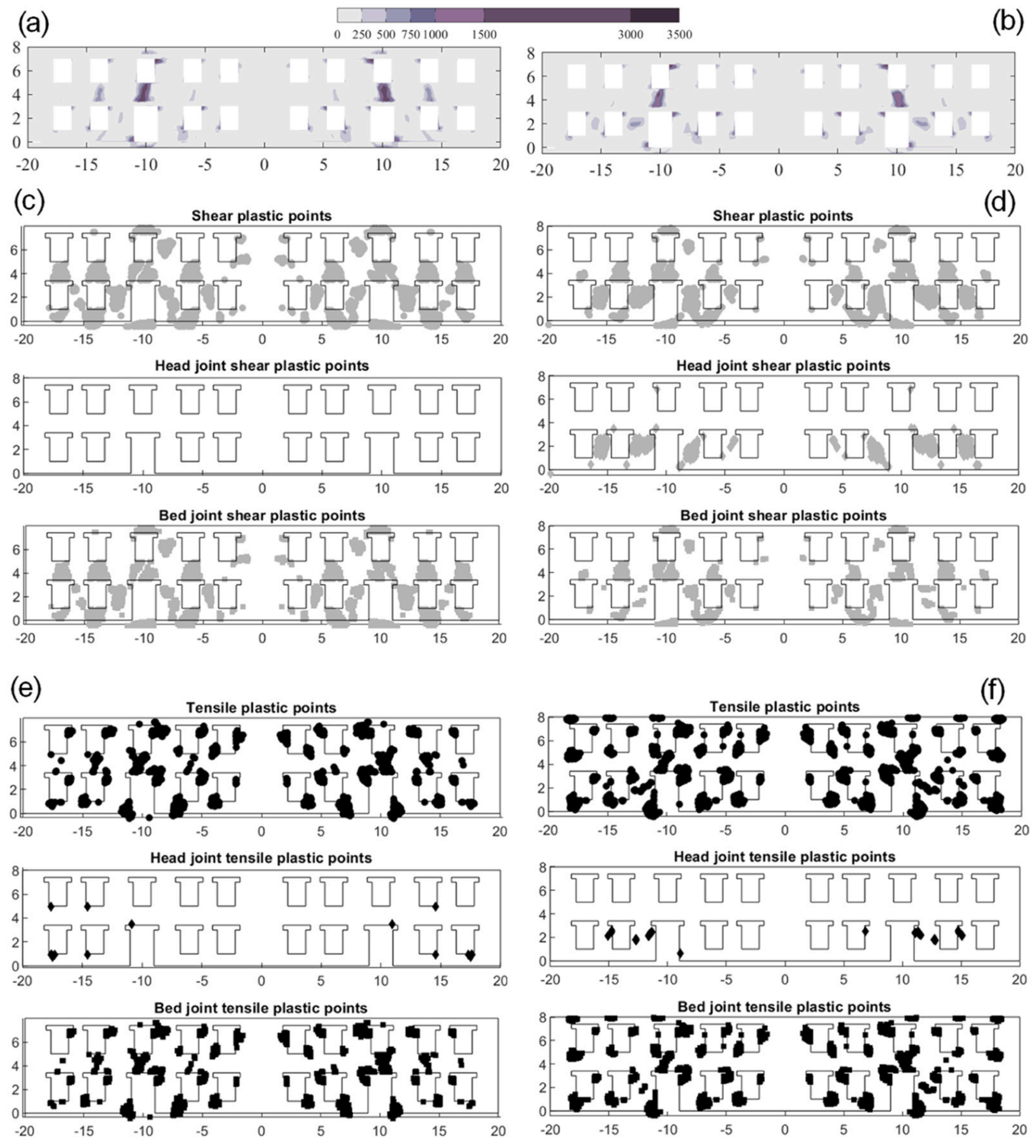

Fig. 18. Maximum principal strain plot at the end of the analysis with (a) JMM and (b) JMM-E model, shear plastic points in case of (c) JMM and (d) JMM-E, tensile plastic points in case of (e) JMM and (f) JMM-E.

the piers located at the ground floor. Inspecting the output in terms of shear plastic points (Fig. 18c and d) it can be noted that the roots of this different damage picture should be found in the systematic overestimation of the head joints shear strength in JMM model, which in turn derives from the analytical formulation already discussed in Section 2. In this case, not many differences arise in the tensile plastic points distribution, reasonably because the compressive stress (σ_{zz}) increment due to self-weight does not cause the attainment of the tensile strength cutoff introduced in the JMM-E formulation, thus the two models provide a very similar pattern of tensile plastic points on both head and bed joints (Fig. 18 e and f).

The case of a four-storey façade provides a more differentiated picture of damage at the end of the tunnel excavation, especially if plastic points are looked at. However, even if both strain plots (Fig. 19 a and b), provide an overall damage category estimate of slight to moderate, strain concentration mainly involves spandrels in the case of JMM simulations, while slight damage also appears on piers, especially at the lower storeys, in JMM-E simulations. Plastic points associated to shear failure predominantly concentrate in spandrels and are solely associated to bed joints failure in the case of JMM (Fig. 19c), while the JMM-E model captures shear yielding on head joints too, especially on the piers, where this orientation governs the structural response. Tensile yielding appears to be strongly influenced in this case by the constitutive model assumptions. As Fig. 19 e and f clearly demonstrate, very few points attain tensile failure on head joints orientation when JMM is adopted, while diffused tensile plastic points appear on the head joints orientation in the case of JMM-E, and these are mostly located around the openings, where cracks are likely to initiate.

Albeit simple and possibly non-exhaustive, this idealised engineering problem highlights that the improvement associated with the enriched model lies in both a quantitative and a qualitative prediction of the damage experienced by masonry structures subjected, as an example, to settlements. This is sought to be a clear advantage as more detailed damage descriptions (attainable by means of plastic points categorisation) are considered essential to design preventive monitoring and protection for structures considered at risk, and to assess possible retrofitting strategies.

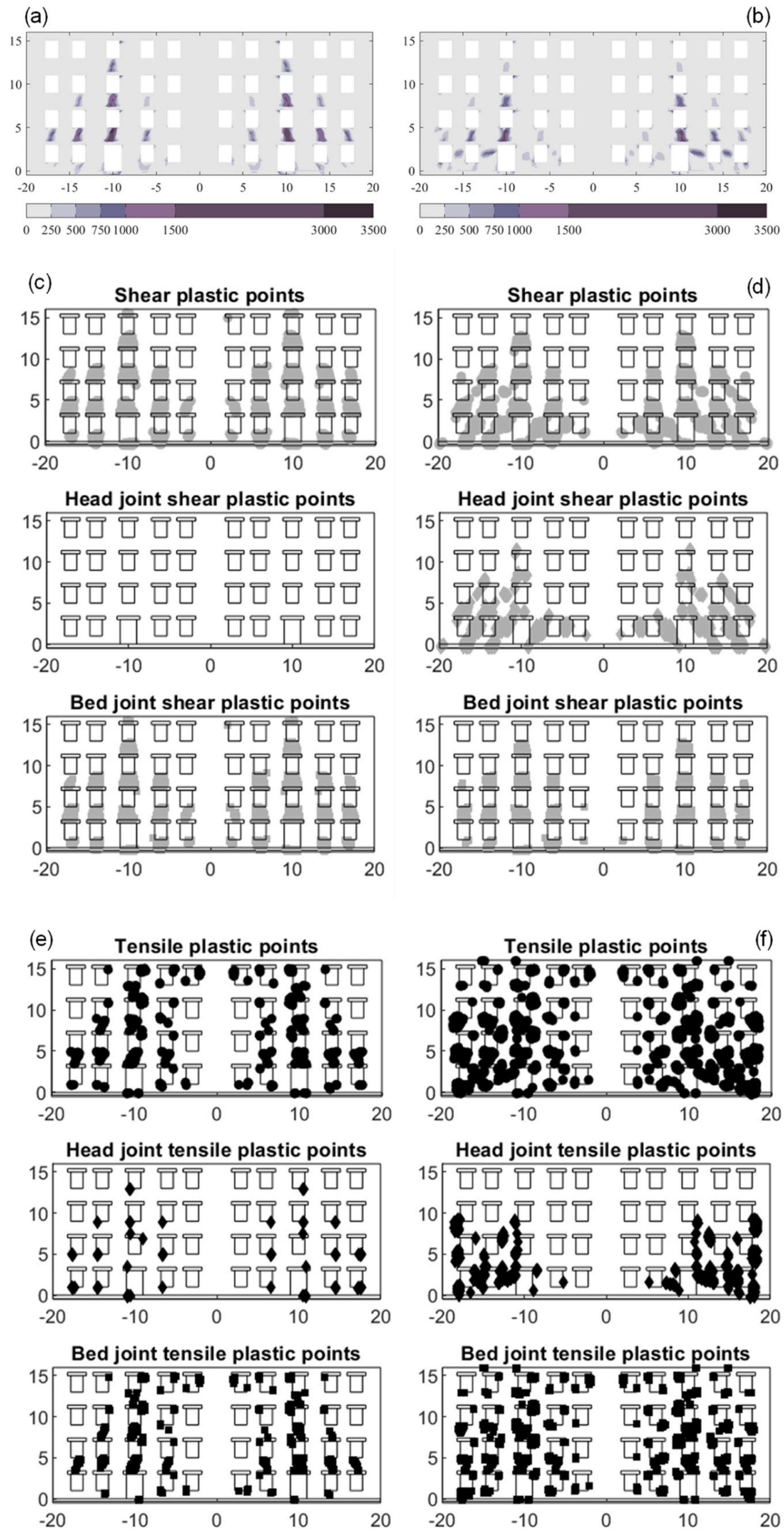

Fig. 19. Maximum principal strain plot at the end of the analysis with (a) JMM and (b) JMM-E model, shear plastic points in case of (c) JMM and (d) JMM-E, tensile plastic points in case of (e) JMM and (f) JMM-E.

7. Conclusions

This paper presents the formulation and applications of an enriched, phenomenologically based constitutive model for masonry: the JMM-E. Building on its predecessor, JMM, the new model retains the core hypotheses that validate the multilaminate idealisation for regularly bonded brick masonry. It assumes an elastic-perfectly plastic behaviour with fixed failure orientations aligned with the bed and head joints.

Compared to JMM, the JMM-E model introduces a more mechanically grounded interpretation of the yield domains and their evolution based on the current stress state, incorporating phenomenological insights. The result is a constitutive framework that relies on a limited number of parameters, each with a clear mechanical meaning and unambiguous calibration, provided that appropriate standard tests are available. This simplicity in parameter identification distinguishes JMM-E from many advanced constitutive models, which often require complex non-standard testing and ad-hoc, sometimes unclear, calibration processes that can deter from their common use.

JMM-E was implemented in a commercial finite element code and first validated through simulations carried out on representative elements of volume, to highlight its capabilities and fundamental differences compared to the JMM. Subsequently, simulations of real experiments on plain and windowed masonry walls were conducted. Notably, all input parameters used in these simulations were derived from standard, well-documented tests. The proposed calibration procedure, formulated for both existing and new masonry constructions, emphasises the ease of its usage in practical problems.

Importantly, the JMM-E model is intentionally designed as a relatively simple yet robust tool for applications in soil-structure interaction problems, particularly in tunnelling contexts. In such applications, it is critical to represent the structural and soil behaviour with reasonable accuracy while maintaining computational efficiency. This necessitates a certain degree of simplification in the structural model to better accommodate the inherent complexity of the soil-structure system. Accordingly, the model does not incorporate cyclic degradation induced by loading behaviour in terms of post-yield stiffness degradation. This is a deliberate choice that does not imply serious inaccuracies, given that tunnelling-induced ground deformations typically induce monotonic loading, where unloading and reloading effects are minimal. On the other hand, absence of cyclic degradation mechanisms limits the model's accuracy under dynamic conditions (such as those encountered during seismic events). While this feature is a tolerable compromise in static, monotonic scenarios, in cyclic applications the model's elastic-perfectly plastic nature may lead to unrealistic hysteresis loops and consequent overestimation of energy dissipation.

The Authors acknowledge this limitation and are currently investigating extensions aimed at accounting for post-yielding and cyclic degradation effects. These future developments will also address known challenges such as the non-objectivity and mesh dependency of the solution, systematically associated with softening models.

CRediT authorship contribution statement

Angelo Amorosi: Writing – review & editing, Supervision, Resources, Project administration, Funding acquisition, Conceptualization. **Giacomo Di Santo:** Writing – review & editing, Visualization, Software, Formal analysis, Data curation. **Marialuigia Sangirardi:** Writing – review & editing, Writing – original draft, Visualization, Validation, Supervision, Software, Methodology, Investigation, Formal analysis, Data curation, Conceptualization.

Declaration of Competing Interest

The authors declare that they have no known competing financial interests or personal relationships that could have appeared to influence the work reported in this paper.

Acknowledgments

The Authors acknowledge the financial support under the National Recovery and Resilience Plan (NRRP), Mission 4, Component 2, Investment 1.1, Call for tender No. 1409 published on 14.9.2022 by the Italian Ministry of University and Research (MUR), funded by the European Union - NextGenerationEU - Project Title DAMAGE, Prin 2022 - CUP B53D23005430006 - Grant Assignment Decree No. 961 adopted on 30/06/2023 by the Italian Ministry of Ministry of University and Research (MUR).

Data availability

Data will be made available on request.

References

[1] Page A. The biaxial compressive strength of brick masonry. Proc Inst Civ Eng 1981; 71:893–906.
[2] Page A. The strength of brick masonry under biaxial tension-compression. Int J Mason Constr 1983;3:26–31.
[3] Pietruszczak S, Ushaksaraei R. Description of inelastic behaviour of structural masonry. Int J Solids Struct 2003;40:4003–19.
[4] D'altri AM, Sarhosis V, Milani G, Rots J, Cattari S, Lagomarsino S, et al. Modeling strategies for the computational analysis of unreinforced masonry structures: review and classification. Arch Comput Methods Eng 2020;27:1153–85.
[5] Hua Y, Buzzetti M, Pingaro N, da Silva LC, Milani G. A computerized tool for the kinematic limit analysis of 2D masonry structures failing on a tilting table. SoftwareX 2025;30:102180.
[6] D'Altri AM, De Miranda S, Castellazzi G, Sarhosis V. A 3D detailed micro-model for the in-plane and out-of-plane numerical analysis of masonry panels. Comput Struct 2018;206:18–30.
[7] Minga E, Macorini L, Izzuddin BA. A 3D mesoscale damage-plasticity approach for masonry structures under cyclic loading. Meccanica 2018;53:1591–611.
[8] Petracca M, Pelà L, Rossi R, Zaghi S, Camata G, Spacone E. Micro-scale continuous and discrete numerical models for nonlinear analysis of masonry shear walls. Constr Build Mater 2017;149:296–314.
[9] Berto L, Saetta A, Scotta R, Vitaliani R. An orthotropic damage model for masonry structures. Int J Numer Methods Eng 2002;55:127–57.
[10] Lopez J, Oller S, Onate E, Lubliner J. A homogeneous constitutive model for masonry. Int J Numer Methods Eng 1999;46:1651–71.
[11] Saloustros S, Pelà L, Cervera M, Roca P. An enhanced finite element macro-model for the realistic simulation of localized cracks in masonry structures: a large-scale application. Int J Archit Herit 2018;12:432–47.
[12] Sousamli M, Messali F, Rots JG. A total-strain based orthotropic continuum model for the cyclic nonlinear behavior of unreinforced brick masonry structures. Int J Numer Methods Eng 2022;123:1813–40.
[13] Bertolesi E, Milani G, Casolo S. Homogenization towards a mechanistic Rigid Body and Spring Model (HRBSM) for the non-linear dynamic analysis of 3D masonry structures. Meccanica 2018;53:1819–55.
[14] Calderini C, Lagomarsino S. Continuum model for in-plane anisotropic inelastic behavior of masonry. J Struct Eng 2008;134:209–20.
[15] Cavalagli N, Cluni F, Gusella V. Strength domain of non-periodic masonry by homogenization in generalized plane state. Eur J MechA/Solids 2011;30:113–26.
[16] Cecchi A, Sab K. A homogenized Reissner–Mindlin model for orthotropic periodic plates: Application to brickwork panels. Int J Solids Struct 2007;44:6055–79.
[17] De Buhan P, De Felice G. A homogenization approach to the ultimate strength of brick masonry. J Mech Phys Solids 1997;45:1085–104.
[18] Zucchini A, Lourenço PB. A micro-mechanical model for the homogenisation of masonry. Int J Solids Struct 2002;39:3233–55.
[19] Schiavoni M, Giordano E, Roscini F, Clementi F. Advanced numerical insights for an effective seismic assessment of historical masonry aggregates. Eng Struct 2023; 285:115997.
[20] Monaco AL, Grillanda N, Onescu I, Fofiu M, Clementi F, D'Amato M, et al. Seismic assessment of Romanian Orthodox masonry churches in the Banat area through a multi-level analysis framework. Eng Fail Anal 2023;153:107539.
[21] Gatta C, Addessi D. Orthotropic multisurface model with damage for macromechanical analysis of masonry structures. Eur J MechA/Solids 2023;102: 105077.
[22] Lourénço PB, De Borst R, Rots JG. A plane stress softening plasticity model for orthotropic materials. Int J Numer Methods Eng 1997;40:4033–57.
[23] Pelà L, Cervera M, Oller S, Chiumenti M. A localized mapped damage model for orthotropic materials. Eng Fract Mech 2014;124:196–216.
[24] Pande GN, Sharma K. Multi-laminate model of clays—a numerical evaluation of the influence of rotation of the principal stress axes. Int J Numer Anal Methods Geomech 1983;7:397–418.
[25] Pietruszczak S, Niu X. A mathematical description of macroscopic behaviour of brick masonry. Int J Solids Struct 1992;29:531–46.
[26] Pietruszczak S, Pande G. Multi-laminate framework of soil models—plasticity formulation. Int J Numer Anal Methods Geomech 1987;11:651–8.

[27] A. Azami, T. Yacoub, J. Curran, Effects of strength anisotropy on the stability of slopes, in: 65th Canadian Geotechnical Conference, CGS Geo-Manitoba, Winnipeg, Manitoba, Canada, 2012.
[28] Goodman RE, Taylor RL, Brekke TL. A model for the mechanics of jointed rock. J Soil Mech Found Div 1968;94:637–59.
[29] Lasciarrea WG, Amorosi A, Boldini D, De Felice G, Malena M. Jointed Masonry Model: A constitutive law for 3D soil-structure interaction analysis. Eng Struct 2019;201:109803.
[30] Atkinson RH, Noland JL, Proposed A. Failure theory for brick masonry in compression. 1983. p. 5.1–7. Proceedings of the 3rd Canadian Masonry Symposium, Edmonton, Canada.
[31] Atkinson RH, Noland JL, Abrams DP, McNary S. A deformation failure theory for stack-bond brick masonry prism in compression. 1985. p. 577–92. Proceedings of the 7th International Brick Masonry Conference, Melbourne, Australia.
[32] Atkinson RH, Noland JL, Abrams DP, McNary S. A deformation failure theory for stack-bond brick masonry prisms in compression. 1985. p. 18.1–18.18. Proceeding of the 3rd North America Masonry Conference, Colorado, USA.
[33] Drysdale RG, Hamid AA. Behavior of concrete block masonry under axial compression. 1979. p. 707–22. Journal Proceedings.
[34] Hamid AA, Drysdale RG. Suggested failure criteria for grouted concrete masonry under axial compression. 1979. p. 1047–62. Journal Proceedings.
[35] Amorosi A, Sangirardi M. Coupled three-dimensional analysis of the progressive tunnelling-induced damage to masonry buildings: is it always worth it? Tunn Undergr Space Technol 2021;118:104173.
[36] Sangirardi M, Amorosi A, de Felice G. A coupled structural and geotechnical assessment of the effects of a landslide on an ancient monastery in Central Italy. Eng Struct 2020;225:111249.
[37] Zhang X, Qu H, Xu Y, Zhang L, Zhang Z. Investigating the damage to masonry buildings during shield tunneling: a case study in Hohhot Metro. Eng Fail Anal 2024;160:108147.
[38] de Felice G, Amorosi A, Malena M. Elasto-plastic analysis of block structures through a homogenization method. Int J Numer Anal Methods Geomech 2010;34: 221–47.
[39] Esposito R, Messali F, Rots JG. Tests for the characterization of replicated masonry and wall ties. Delft: Delft University of Technology; 2016. p. 353–65.
[40] R. Brinkgreve, S. Kumarswamy, W. Swolfs, D. Waterman, A. Chesaru, P. Bonnier, others, PLAXIS 2016, PLAXIS Bv, the Netherlands (2016) 1–16.
[41] G. Ravenshorst, F. Messali, Out-of-plane tests on replicated masonry walls, Delft University of Technology. Final Report 29 (2016).
[42] American Society for Testing and Materials (ASTM), ASTM C597 - Standard Test Method for Pulse Velocity Through Concrete, (2010).
[43] American Society for Testing and Materials (ASTM), ASTM E1876 - Standard Test Method for Dynamic Young's Modulus, Shear Modulus, and Poisson's Ratio by Impulse Excitation of Vibration, (2002).
[44] Makoond N, Cabané A, Pelà L, Molins C. Relationship between the static and dynamic elastic modulus of brick masonry constituents. Constr Build Mater 2020; 259:120386.
[45] Makoond N, Pelà L, Molins C. Dynamic elastic properties of brick masonry constituents. Constr Build Mater 2019;199:756–70.
[46] Ozdemir A, Sangirardi M, Judd M, Acikgoz S. Evaluation of test procedures and correlations for the mechanical characterisation of brick masonry and its constituents. Constr Build Mater 2025;489:142133.
[47] Sangirardi M, Judd MR, Ozdemir A, Acikgoz S. Strain-level dependency in static and dynamic Young's moduli characterisation of hydraulic lime mortars. RILEM Technical Letters 2025;10:98–105.
[48] American Society for Testing and Materials (ASTM), ASTM C803 - Standard Test Method for Penetration Resistance of Hardened Concrete, (2018).
[49] European Standards, EN 14488-2: Testing sprayed concrete - Part 2: Compressive strength of young sprayed concrete, (2006).
[50] Chen W-F. Double punch test for tensile strength of concrete. 1970. p. 993–5. Journal Proceedings.
[51] American Society for Testing and Materials (ASTM), ASTM C1197 - Standard Test Method for In Situ Measurement of Masonry Deformability Properties Using the Flatjack Method, (2022).
[52] European Standards, EN 1052-3: Methods of test for masonry - Part 3: Determination of initial shear strength, (2002).
[53] Liu B, Drougkas A, Sarhosis V, Smith CC, Gilbert M. Experimental investigation on the shear behaviour of the brickwork-backfill interface in masonry arch bridges. Eng Struct 2023;292:116531.
[54] American Society for Testing and Materials (ASTM), ASTM C1357 - Standard Test Methods for Evaluating Masonry Bond Strength, (2009).
[55] American Society for Testing and Materials (ASTM), ASTM C952 - Standard Test Method for Bond Strength of Mortar to Masonry Units, (2012).
[56] American Society for Testing and Materials (ASTM), ASTM C1072 - Standard Test Methods for Measurement of Masonry Flexural Bond Strength, (2022).
[57] European Standards, EN 1052-5: Methods of test for masonry - Part 5: Determination of bond strength by the bond wrench method, (2005).
[58] Khalaf FM. New test for determination of masonry tensile bond strength. J Mater Civ Eng 2005;17:725–32.
[59] American Society for Testing and Materials (ASTM), ASTM C1531 - Standard Test Methods for In Situ Measurement of Masonry Mortar Joint Shear Strength Index, (2022).
[60] Jafari S, Rots JG, Esposito R. A correlation study to support material characterisation of typical Dutch masonry structures. J Build Eng 2022;45:103450.
[61] J.G. Rots, Structural masonry: an experimental/numerical basis for practical design rules, 1997.
[62] Vermeltfoort AT, Raijmakers T, Janssen HJM. Shear tests on masonry walls. In: Hamid AA, Harris HG, editors. Proceedings of the 6th North American Masonry Conference. Philadelphia, Pennsylvania, USA: Technomic Publ. Co.; 1993. p. 1183–93.
[63] P.J.B.B. Lourenço, Computational strategies for masonry structures., (1997).
[64] Boscardin MD, Cording EJ. Building response to excavation-induced settlement. J Geotech Eng 1989;115:1–21.
[65] Di Santo G, Sangirardi M, Amorosi A. Numerical modelling of the influence of masonry building stiffness and irregularity on tunnelling induced damage. 2025. Structural Analysis of Historical Constructions SAHC, Volume 1, Lausanne.